

Article

Hydrothermally Synthesized Cerium Phosphate with Functionalized Carbon Nanofiber Nanocomposite for Enhanced Electrochemical Detection of Hypoxanthine

Prashant K. Kasare and Sea-Fue Wang *

Department of Materials and Mineral Resources Engineering, National Taipei University of Technology, Taipei 106, Taiwan; t112a09402@ntut.edu.tw

* Correspondence: sfwang@ntut.edu.tw

Abstract: This work presents the detection of hypoxanthine (HXA), a purine derivative that is similar to nucleic acids who overconsumption can cause health issues, by using hydrothermally synthesized cerium phosphate (CePO_4) followed by a sonochemical approach for CePO_4 decorated with a functionalized carbon nanofiber ($\text{CePO}_4@f\text{-CNF}$) nanocomposite. The formation of the nanocomposite was confirmed with X-ray powder diffraction (XRD), scanning electron microscopy (SEM), and energy-dispersive spectroscopy (EDS). A $\text{CePO}_4@f\text{-CNF}$ nanocomposite is used to modify a glassy carbon electrode (GCE) to analyze the electrochemical detection of HXA. Cyclic voltammetry (CV), Electrochemical impedance spectroscopy (EIS), and Differential pulse voltammetry (DPV) were used to examine the electrochemical properties of the composite. As a result, the modified electrode exhibits a larger active surface area ($A = 1.39 \text{ cm}^2$), a low limit of detection (LOD) at $0.23 \mu\text{M}$, a wide linear range ($2.05\text{--}629 \mu\text{M}$), and significant sensitivity. Therefore, the $\text{CePO}_4@f\text{-CNF}$ nanocomposite was used to study the real-time detection in chicken and fish samples, and it depicted significant results.

Keywords: hypoxanthine; cerium phosphate; functionalized-carbon nanofiber; modified electrode; hydrothermal approach



Citation: Kasare, P.K.; Wang, S.-F. Hydrothermally Synthesized Cerium Phosphate with Functionalized Carbon Nanofiber Nanocomposite for Enhanced Electrochemical Detection of Hypoxanthine. *Chemosensors* **2024**, *12*, 84. <https://doi.org/10.3390/chemosensors12050084>

Received: 18 April 2024

Revised: 9 May 2024

Accepted: 13 May 2024

Published: 16 May 2024



Copyright: © 2024 by the authors. Licensee MDPI, Basel, Switzerland. This article is an open access article distributed under the terms and conditions of the Creative Commons Attribution (CC BY) license (<https://creativecommons.org/licenses/by/4.0/>).

1. Introduction

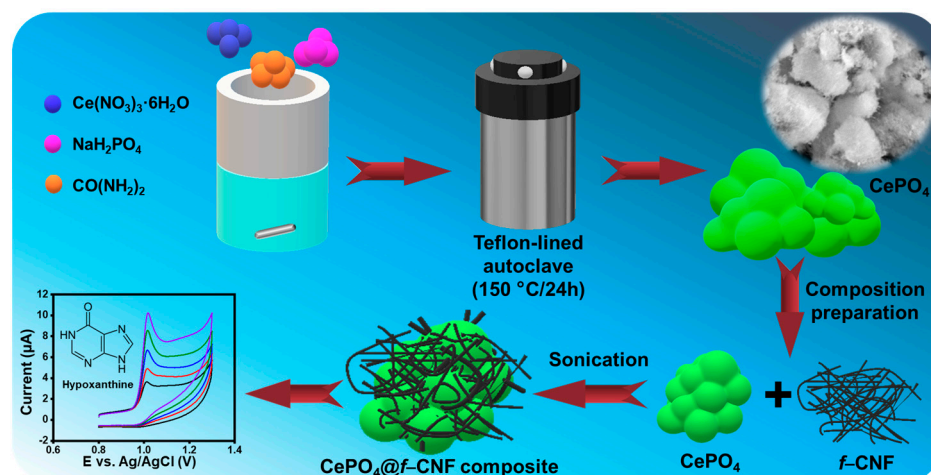
Hypoxanthine (HXA: 1, 7-dihydro-6H-purine-6-one) is a degradation of purine metabolism in the animal and human body [1]. It helps with the synthesis of purine nucleotides, which are essential building blocks of DNA and RNA [2]. It is produced during the purine metabolism, and it is transformed from xanthine (XN) to uric acid (UA), along with the production of reactive oxygen species (ROS), with the action of the enzyme xanthine oxidase (XO) [1]. The microbial decomposition of adenosine triphosphate (ATP) produces uric acid (UA) in this human serum degradation step [3]. There is an abundant concentration of hypoxanthine in chicken and fish food products, which can be easily detectable [4]. Its small, polar, stable shape makes it easy to accumulate in biological tissues and fluids [1]. Purines, including HXA, can act as signaling molecules in various cellular processes, and they are involved in neurotransmission and other signaling pathways. Purine metabolism abnormalities, including excess hypoxanthine levels, can be causally associated with metabolic disorders such as Lesch–Nyhan syndrome [5]. Since the presence of HXA in our extracellular fluids has caused some diseases, including xanthinuria, goat, urolithiasis, joint inflammation, hyperuricemia, kidney failure, Alzheimer's, etc., because of these reasons, the detection and quantity measurement of HXA has become increasingly important [3,6]. Also, fish and chicken foods are important elements of a healthy diet, and global requirements are increasing for fresh and packed meat foodstuffs. Food freshness and safety are major issues for consumers and are challenging for the food industries. The existence of HXA serves as an effective biomarker to predict the degradation and quality of

food, and if it is used in high concentrations, may cause animal death and the durability of storage [7]. Also, the measurement of HXA levels is extremely important in meat-based products for clinical diagnosis and quality controls.

There are many conventional techniques used to analyze the HXA, including fluorescence spectroscopy [8], spectrophotometry [9], gas chromatography-mass spectrometry (GCMS) [10], and high-performance liquid chromatography (HPLC) [10]. Among these conventional techniques, electrochemical sensors are an affordable method due to taking less time to detect, their friendly nature, and their low cost, etc. Electrochemical studies show excellent redox behavior, oxygen storage capacity, catalytic activity, and versatility, which makes it a valuable component. In general, electrochemical sensors are capable of detecting many different kinds of metal ions, natural substances, and organic and inorganic compounds. It is used in different kinds of sectors, including environmental and biological monitoring and industry. Modified electrodes also possess an important role in the electrochemical technique, because the electrochemical analyzing system is deficient in exact detection caused by its high overpotential desire, interference from contaminants, and reversibility, all of these represent significant analytical challenges [11]. On the other hand, the modified electrodes show tremendous active sites, good stability, and excellent sensitivity. They are rich in possibilities to modify the working electrode active surface area using materials, including several nanoparticles, inorganic and organic redox agents, metal oxides, metal sulfides, metal nitrides, polymers, carbon materials, etc. [11].

Lanthanides have specific electronic structures and similar inner 4f electronic energy levels [12]. Among the lanthanide compounds, Cerium phosphate (CePO_4) has remarkable properties, which include stability, nontoxicity, huge surface area, and good ion conductivity. In addition, the Ce element's charge valence can be shifted between +3 and +4, resulting in its high redox conversion capacity [13]. Metal phosphate (CePO_4) is extensively utilized in various applications like catalysis [14], sensors [15], solar cells [16], and supercapacitors [17]. Carbonous materials have high surface area, cavities, and micropores, which include graphene oxides (GO), graphitic carbon nitrate (GCN), carbon nanotubes (CNT), carbon nanodots, and carbon nanofibers (CNF), which are widely acknowledged as outstanding conductive composite materials that attract considerable attention [11]. Since CNF compounds with superior charge transfer have the potential to accelerate electron and ion transfer substantially, they can improve the modified electrode's electrochemical performance [18]. CePO_4 has a large active surface area and superior electrochemical performance, making it an effective electrode material. On the other hand, *f*-CNF offers good conductivity and stability for facilitating electron transfer in electrochemical sensors. Synergistic effects and the electrostatic interaction (π - π —interaction) between CePO_4 and *f*-CNF show enhanced improvement in electrochemical sensors [11]. Functionalization provides higher sensitivity, selectivity, and increased active surface area [19]. Therefore, the *f*-CNF exhibits better redox properties than the pristine CNF. This action was approved by P. Bharathi et al. [20]. Furthermore, this work shows that the $\text{CePO}_4@f\text{-CNF}$ detects the HXA analyte for electrochemical sensor applications.

In this work, the $\text{CePO}_4@f\text{-CNF}$ nanocomposite was formed via a hydrothermal followed sonochemical approach, which was used to prepare a modified electrode to detect HXA, as shown in Scheme 1. The prepared $\text{CePO}_4@f\text{-CNF}$ composite was characterized using morphological and spectroscopic analysis. Additionally, DPV, EIS, and CV were taken to inspect the electrochemical study of the $\text{CePO}_4@f\text{-CNF}$ nanocomposite. The $\text{CePO}_4@f\text{-CNF}$ -modified electrode exhibits enhanced electrochemical activity for hypoxanthine determination in real samples.



Scheme 1. Schematic presentation of the synthesis of CePO_4 and $\text{CePO}_4@f\text{-CNF}$ nanocomposites for the detection of HXA.

2. Experimental Methods

2.1. Preparation of *f*-CNF

The surface of the pristine CNFs was modified or functionalized through acid treatment. Initially, Conc., HNO_3 : H_2SO_4 was made in a 3:1 ratio, and a solution was stirred at $65\text{ }^\circ\text{C}/6\text{ h}$. After naturally cooling down to room temperature, the solution was centrifuged to separate the acidic solution and accumulate the CNF suspension. After that, the solution was washed repeatedly using DI water until the pH reached neutral. Then, it was dried out from a hot air oven at $60\text{ }^\circ\text{C}$ for 20 h [11,21]. The outcome was labeled as *f*-CNF.

2.2. Synthesis of Cerium Phosphate (CePO_4)

All chemicals were taken with an analytical grade, and it was used without purification. $\text{Ce}(\text{NO}_3)_3 \cdot 6\text{H}_2\text{O}$ was used as a cerium source, NaH_2PO_4 was used as a phosphorus source, and $\text{CO}(\text{NH}_2)_2$ was used as a surfactant in the hydrothermal method to synthesize CePO_4 . Firstly, $\text{Ce}(\text{NO}_3)_3 \cdot 6\text{H}_2\text{O}$ and NaH_2PO_4 were added to the exact ratio of 0.1: 0.2 M in 100 mL DI water, After continuous stirring, $\text{CO}(\text{NH}_2)_2$ was added to the mixture, and then stirred for 120 min to acquire a consistent mixture. This homogeneous solution was delivered into a Teflon-coated autoclave and hydrothermally approached for 24 h at $150\text{ }^\circ\text{C}$. It was then left to naturally cool to its ambient temperature. After the last stage of the reaction, centrifugation was used to extract the CePO_4 precipitate from the mixture. Also, multiple DI and ethanol washes were then utilized, and the mixture was dried at $60\text{ }^\circ\text{C}$. The obtained CePO_4 powder was used in all further studies.

2.3. Preparation of $\text{CePO}_4@f\text{-CNF}$

A simple stirring approach method was used to synthesize a cerium phosphate functionalized carbon nanotube ($\text{CePO}_4@f\text{-CNF}$) nanocomposite. The properly prepared CePO_4 and *f*-CNF were introduced in 20 mL of ethanol with a 1:1 weight ratio. In total, 25 min were spent stirring the mixture, and it was then ultrasonicated for 2 h at 100 W and 50 kHz in an ultrasonic bath. The $\text{CePO}_4@f\text{-CNF}$ nanocomposite was dried at $60\text{ }^\circ\text{C}$ to completely evaporate the moisture. The final product was a consistent $\text{CePO}_4@f\text{-CNF}$ powder.

2.4. Preparation of Modified Glassy Carbon Electrode (GCE)

The surface area of GCE was polished mechanically over a velvet micro-cloth and fine alumina powder sludge, and then were washed with distilled water and ethanol after earlier depositing the prepared nanocomposite. In total, 2 mg of the synthesized $\text{CePO}_4@f\text{-CNF}$ nanocomposite was dissolved in 1 mL of ethanol and sonication toward 45 min. Then, approximately $6\text{ mg}/\mu\text{L}$ of the $\text{CePO}_4@f\text{-CNF}$ nanocomposite solution was

dropped over the working electrode and dried out. The modified electrode is represented by $\text{CePO}_4@f\text{-CNF}/\text{GCE}$. Similarly, CePO_4/GCE and $f\text{-CNF}/\text{GCE}$ were developed for electrochemical examination.

2.5. Real Sample Analysis

Chicken and fish products are purchased from a local market and cut into small pieces. Then, 2 gm of small pieces of meat samples were diluted in deionized water by a stirring approach for 60 min and then centrifuged at 10,000 rpm for 10 min. The obtained solution was mixed with 0.1 M PBS (pH = 7.0) with a 1:10 dilution ratio (v/v) [9,22,23].

3. Results and Discussion

3.1. Choice of Material

Transition metal oxides are more frequently used than metal ions. However, particular transition metals, such as Au, Ag, and Pt, are costly, and the sources are minimal. Researchers are trying to develop a technique to derive materials using low-cost transition metals to deal with this issue. Generally, f-block elements, like lanthanides and actinides, are inner transition metals and have good electrical and thermal conductivity. In addition, the Ce element has charge valences that can be shifted between +3 and +4, resulting in its high redox conversion capacity [13]. Metal phosphate (CePO_4) has notable advantages, such as excellent ion conductivity, good active surface area, great stability, a crystal structure, an electronic band structure, and nontoxicity [24]. Similarly, because of their high active surface area, large potential range, low resistivity, and low background current, carbon materials are excellent choices for the fabrication of electrodes.

In this work, the $\text{CePO}_4@f\text{-CNF}$ composite offers a number of active sites from the functionalization of CNF, which enhances chemical reactivity and provides sites for binding with CePO_4 material. In addition, CePO_4 receives great attention due to its unique physiochemical properties and the ability of $\text{Ce}^{3+}/\text{Ce}^{4+}$ to make it a promising material for electrochemical sensors [25]. Hence, this synergism between CePO_4 and $f\text{-CNF}$ enhances its electrochemical performance for HXA determination.

3.2. X-ray Diffraction (XRD) Crystallographic Phase

The XRD analysis of $f\text{-CNF}$, CePO_4 , and $\text{CePO}_4@f\text{-CNF}$ nanocomposite is displayed in Figure 1A. A significant peak can observe the presence of carbon elements at 26.3° which are assigned on the (002) plane of $f\text{-CNF}$ (black) [11,20]. The material demonstrates good crystallinity, purity, and structural properties, as demonstrated by the sharp and clear characteristic peaks of the CePO_4 synthesized in this work. The as-synthesized samples' diffraction peaks correlate with those of the monoclinic CePO_4 (JCPDS-01-077-0429), indicating the space group $P21/n$, with the space group number 14. Furthermore, the $\alpha = \gamma = 90.00^\circ$, $\beta = 103.60^\circ$, and unit cell are $a = 6.77 \text{ \AA}$, $b = 6.99 \text{ \AA}$, and $c = 6.45 \text{ \AA}$. The indexed major XRD peaks appeared at the corresponding lattice planes (111), (111), (200), (120), (012), (202), (112), (130), (103), (212), (132), (023), (322), (132), (140), (014), (124), (513), and there were multiple prominent diffraction peaks found at 2θ values 21.3° , 25.2° , 27° , 28.9° , 31.2° , 34.5° , 36.8° , 41° , 42.1° , 46.2° , 48.6° , 50.8° , 51.9° , 52.6° , 54.2° , 60.4° , 70.2° , and 77.2° , which are matched with the prepared CePO_4 [26]. The peak position ($2\theta^\circ$) and lattice planes' (hkl) values of CePO_4 are shown in Table S1. The $\text{CePO}_4@f\text{-CNF}$ displays all of the specific peaks of CePO_4 that were acquired on behalf of the highly crystalline structure, and the $f\text{-CNF}$ peak overlies with CePO_4 the $f\text{-CNF}$ are not apparent on the nanocomposite XRD. Also, the diffraction peaks of $f\text{-CNF}$ and CePO_4 were used to confirm a successful formation using the sonication method, and $\text{CePO}_4@f\text{-CNF}$ was confirmed using FTIR analysis. Figure 2B shows the crystal structure of the monoclinic formation of CePO_4 (ball-stick model).

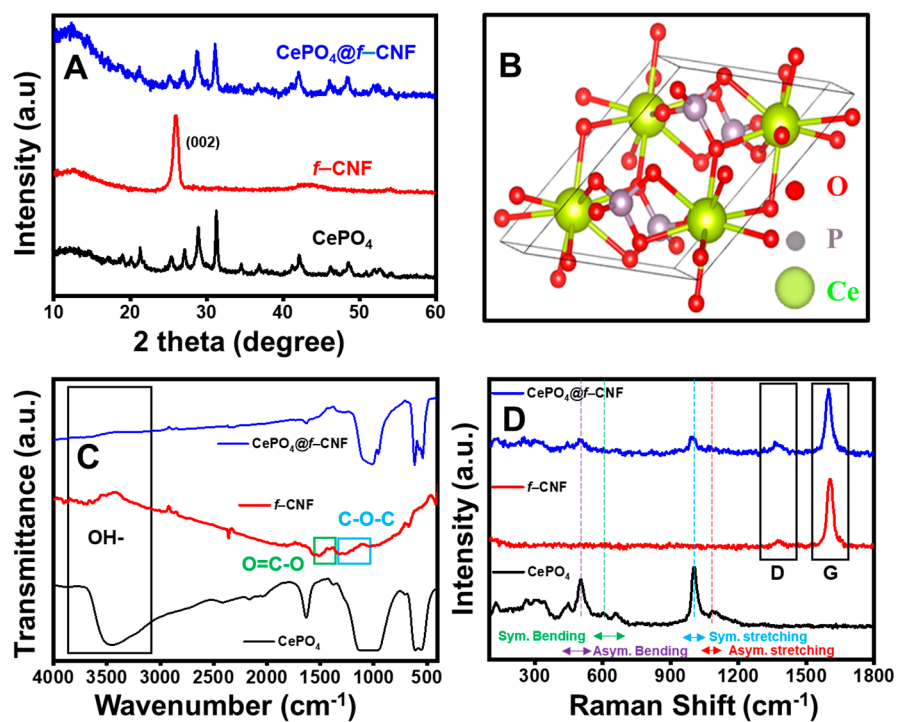


Figure 1. (A) XRD patterns and (B) Crystal structure of CePO₄. (C,D) FTIR and Raman spectra of CePO₄, f-CNF, and CePO₄@f-CNF.

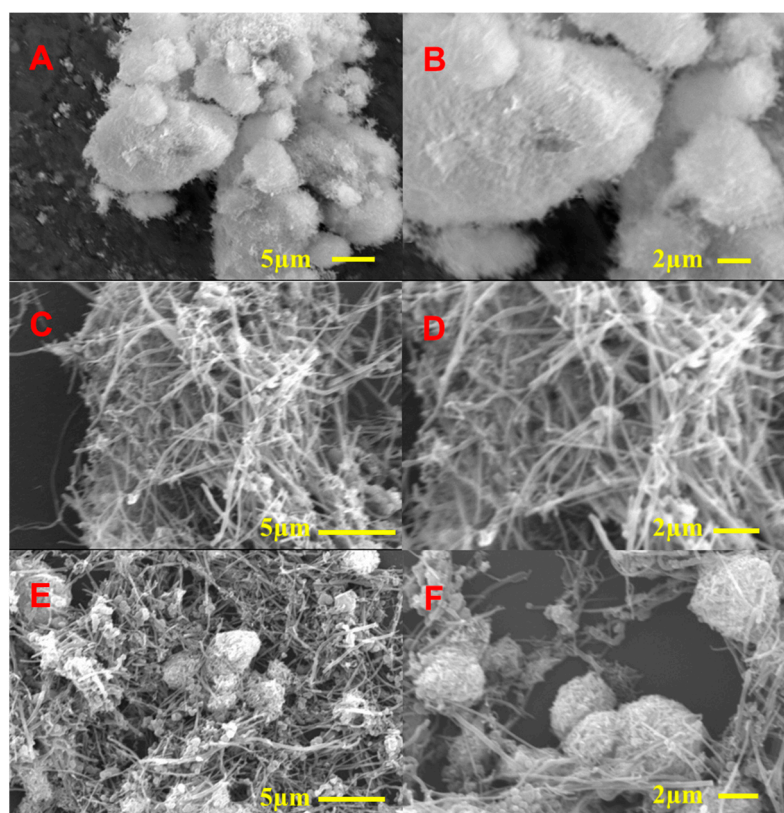


Figure 2. SEM image of (A,B) CePO₄, (C,D) f-CNF, and (E,F) CePO₄@f-CNF nanocomposite.

3.3. FTIR Analysis

FTIR (Fourier transform infrared) spectroscopy is a useful instrument for investigating functional groups and the surfaces of materials. Under some conditions, FTIR spectroscopy is also able to identify surface sites that influence the material's reactivity. To observe the interactions between cerium phosphate and functionalized carbon nanofiber, the FT-IR technique was employed to analyze the chemical structures of CePO_4 , f -CNF, and the $\text{CePO}_4@f$ -CNF composite, shown in Figure 1C, with a range of 500 to 4000 cm^{-1} . f -CNFs exhibited IR bands ranging between 400 to 2000 cm^{-1} , which corresponded to the stretching wavelengths of $-\text{CH}$, and $\text{C}-\text{O}$ [11] in the FTIR spectrum, corresponding to the bending vibration of the PO_4 bands obtained between 530–620 cm^{-1} , and corresponding to the stretching vibrations of the PO_4 bands visible between 950–1100 cm^{-1} [27]. In the O-H group of organic compounds, a peak is observed at nearly 3500 cm^{-1} , which may represent an indication of moisture absorption.

3.4. Raman Analysis

The Raman spectra of CePO_4 , f -CNF, and $\text{CePO}_4@f$ -CNF were analyzed to determine the phase purity, as shown in Figure 1D. The vibration bands represented symmetric bending (δ_s) at ~ 420 – 530 cm^{-1} and asymmetric bending (δ_{AS}) at ~ 580 – 670 cm^{-1} of Raman shift of the P-O Bands. Similarly, the two bands at ~ 1000 and ~ 1100 cm^{-1} in the spectrum determine the symmetric stretching (ν_s) and asymmetric stretching (ν_{AS}) vibrations of the P-O band of the prepared sample [28]. Also, Raman spectroscopy has become extensively used for the verification of carbon-based substances, detecting irregular structures and formations in carbon materials. The C-C stretching of graphitic structure and sp^2 -bonded sites are responsible for the D and G bands seen in f -CNF at ~ 1360 and ~ 1600 cm^{-1} , respectively. Furthermore, the Raman spectra of the $\text{CePO}_4@f$ -CNF nanocomposite show all the essential bands to identify their good formation of the corresponding composite [29].

3.5. Morphological Analysis

The SEM characterization studies, shown in Figure 2, evidently demonstrate the surface morphology of f -CNF, CePO_4 , and $\text{CePO}_4@f$ -CNF. It is widely acknowledged that the geometry of a substance has an impact on its electrochemical performance. Figure 2A,B show the SEM images of hydrothermally synthesized CePO_4 , a sponge-like morphology with numerous irregular agglomerated particles which provide a higher curvature surface. The fiber structure of f -CNF can be observed in the SEM image shown in Figure 2C,D. It shows that the network-like architecture resulting from the interconnection between these nanofibers improves both conductivity and sensing functions. The synthesized $\text{CePO}_4@f$ -CNF nanocomposite's SEM image, which is displayed in Figure 2E,F, exhibits CePO_4 accumulated in carbon f -CNFs. This verified that $\text{CePO}_4@f$ -CNF nanocomposites were successfully synthesized. The increased interaction between CePO_4 and f -CNFs when they are dispersed also contributes to increased electrocatalytic performance and synergism. An analysis of the atomic element distribution in the nanocomposite has been performed using elemental mapping. The composition of elements of the $\text{CePO}_4@f$ -CNF nanocomposite is displayed in Figure 3A–F, as established using EDS analysis. The presence of Ce, O, P, and C atoms indicates the successful configuration of the nanocomposite.

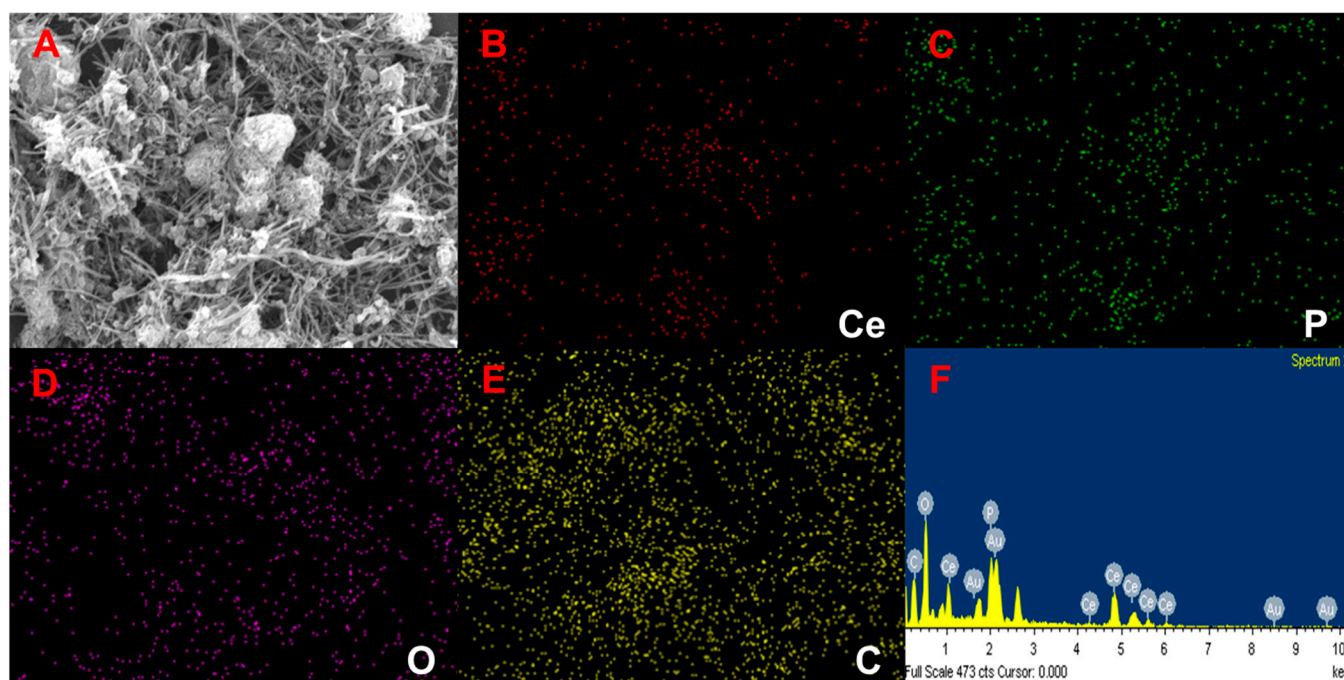


Figure 3. (A–F) SEM image and EDS of CePO₄@*f*-CNF.

3.6. Electrochemical Measurement

Electrochemical Impedance Spectroscopy (EIS) and Cyclic Voltammetry (CV)

Electrochemical impedance spectroscopy (EIS) was utilized to investigate the interfacial charge transfer kinetics, conductivity, and impedance behavior of the modified GCEs (labelled CePO₄/GCE, *f*-CNF/GCE, and CePO₄@*f*-CNF/GCE, respectively) shown in Table S1. EIS was executed in a 5 mM [Fe(CN)₆]^{3−/4−} containing 0.1 M KCl solution. The R_s and R_{ct} (electrolyte resistance and charge transfer resistance) were examined using Randles equivalent circuit model to fit the observed data and examine analysis, as displayed in Figure 4A. Moreover, Nyquist plots are used for EIS measurements for R_{ct}, which are represented as semi-circles arranged in parallel on the electrode surface as an outcome of the electrode impedance. CePO₄@*f*-CNF/GCE expresses a straight line in a low-frequency region and a short semicircle of R_{ct} = 253.24 Ω·cm² in the high-frequency region, indicating that mass diffusion limiting factors regulate the electron transfer mechanism. Along with this, the R_{ct} values of the *f*-CNF/GCE and CePO₄/GCE show 331.82 Ω·cm² and 767.87 Ω·cm², respectively, and the width of the semicircle represents the charge transfer resistance at the electrode surface considerably greater. Here, the CePO₄@*f*-CNF/GCE modified electrode's R_{ct} value shows up to be lower than that of the *f*-CNF/GCE- and CePO₄/GCE-modified electrodes, which perfectly demonstrates that the nanocomposite-modified electrodes exhibit lower diffusion of resistance and charge-transfer resistance, displayed in Table S2.

The CePO₄/GCE, *f*-CNF/GCE, and CePO₄@*f*-CNF/GCE cyclic voltammetry (CV) curves in 0.1 M KCl solution with 5 mM [Fe(CN)₆]^{3−/4−} (scan rate: 50 mV/s) are shown in Figure 4B [30]. CePO₄@*f*-CNF/GCE has the maximum peak current and the lowest peak potential difference ($\Delta E_p = E_{pa} - E_{pc}$) due to the highest level of charge transport efficiency. Figure 4C demonstrates several scan rate studies from 0.02 to 0.2 V/s in 5 mM [Fe(CN)₆]^{3−/4−}. At increasing various scan rates, the anodic peak currents increased significantly. Figure 4D illustrates the linear correlation between the square root of the scan rate and the redox peak current response, The linearity of the two scales has $y = 515.32x + 10.374$ and $y = -399.97x - 22.6$, and the R² values are 0.9991 and 0.9988, accordingly. In conclusion, the remarkable electrochemical redox activity of the recently prepared

CePO₄@*f*-CNF/GCE demonstrated a large active surface area of 1.39 cm², determined using the Randle's–Sevcik equation (Equation (1)).

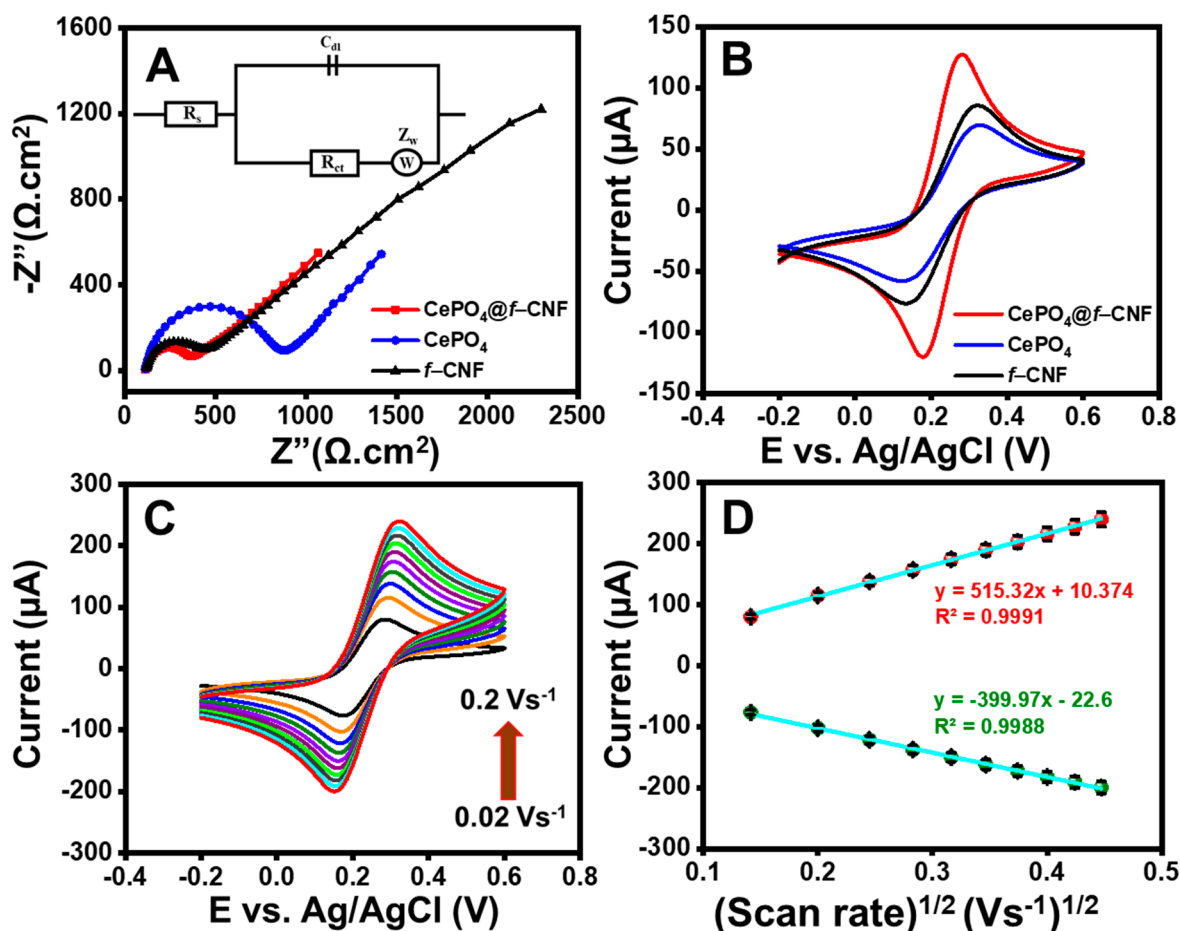


Figure 4. (A) EIS (the Nyquist plot (inset; Randle's circuit model), (B) and CV scan of *f*-CNF/GCE, CePO₄/GCE, and CePO₄@*f*-CNF/GCE. (C) CV curves of CePO₄@*f*-CNF/GCE at different scan rates (0.02–0.2 Vs⁻¹). (D) Linear fitting graph for different scan rates.

$$I_p = 2.69 \times 10^5 n^3 AD^{1/2} Cv^{1/2} \quad (1)$$

3.7. Electrochemical Behaviors of Electrodes

3.7.1. Different Modified Electrodes towards Hypoxanthine

The CV technique was investigated to determine the electrochemical performance of the different modified electrodes in the presence of 100 μM HXA in 0.1 M PBS. However, oxidation peak currents have been observed to be significantly enhanced in each case. In the electrochemical characteristics of bare GCE, CePO₄/GCE, *f*-CNF/GCE, and the prepared nanocomposite CePO₄@*f*-CNF/GCE have been assessed, which achieved the highest peak current relative to the other electrodes shown in Figure 5A. Because of the high surface area and flow of electrons, Hypoxanthine is an acknowledged purine molecule, showing adsorptive abilities at certain electrode surfaces. Furthermore, large oxidation current response peaks against hypoxanthine detection are observed in all of the modified electrodes. The surface of the modified electrode can absorb hypoxanthine when it is added to the PBS electrolyte. The heterojunction formation and synergetic effects are responsible for this most intense anodic peak current within the *f*-CNF/GCE and CePO₄/GCE. The synthesized nanocomposite CePO₄@*f*-CNF/GCE is superior to the other modified electrodes for the detection and optimizations of hypoxanthine with the oxidation

peak potential at 1.02 V and the highest oxidation peak current intensity of 11.98 μA . The corresponding various electrodes with the peak current bar diagram in Figure 5B prove that, compared to the other control materials, composites show the highest peak current. These results suggest that the modified $\text{CePO}_4/f\text{-CNF}$ nanocomposite electrode is appropriate to use for the electrochemical detection of Hypoxanthine.

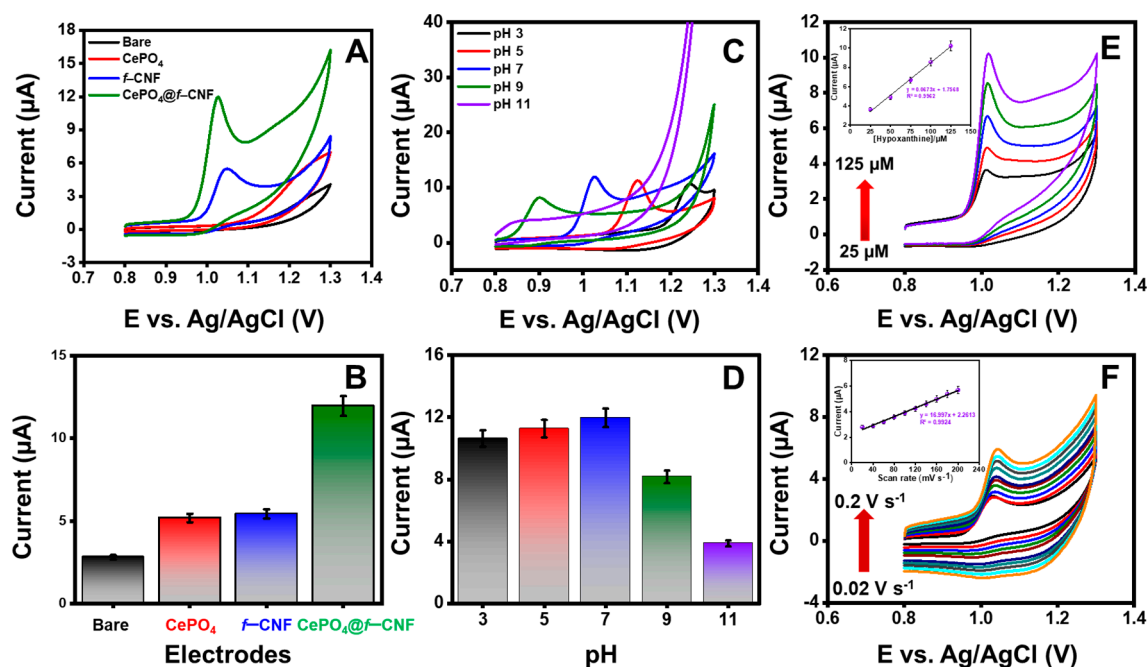


Figure 5. (A,B) CV profile of bare GCE, $f\text{-CNF}/\text{GCE}$, CePO_4/GCE , and $\text{CePO}_4/f\text{-CNF}/\text{GCE}$ in 0.1 M PB (pH-7), with the existence of 100 mM HXA and the relative histogram of electrode towards the current. (C,D) CV curves of the $\text{CePO}_4/f\text{-CNF}/\text{GCE}$ at various electrolyte pH values (0.1 M PB pH 5–9), with the corresponding bar diagram of pH towards the current (mA). (E) CV scan of the $\text{CePO}_4/f\text{-CNF}/\text{GCE}$ with different concentrations from 25 to 125 μM HXA, and the respective (insert) linearity plot of different concentrations. (F) CV curves of the $\text{CePO}_4/f\text{-CNF}/\text{GCE}$ at different scan rates in the presence of 100 mM HXA; the inset is the corresponding linear plot for different scan rates.

3.7.2. Effect of Different Loadings

The optimization test was performed using multiple loading concentrations to determine the most suitable catalytic loading amount. In Figure S1A,B, CV determines the result of the $\text{CePO}_4/f\text{-CNF}/\text{GCE}$ at different loading amounts of 4 to 8 $\text{mg}/\mu\text{L}$, and was used for drop-casting in 100 μM HXA in 0.1 M PB (pH-7.0). The lowest current, 3.01 μA , was obtained at 4 $\text{mg}/\mu\text{L}$ of $\text{CePO}_4/f\text{-CNF}/\text{GCE}$. In total, 4 $\text{mg}/\mu\text{L}$ of modified electrode, demonstrated in a less active site and less current that the electrode's surface was not completely coated with the $\text{CePO}_4/f\text{-CNF}$ nanocomposite. Therefore, the huge current was detected with a 6 $\text{mg}/\mu\text{L}$ loading amount of 11.98 μA . The oxidation current response rises gradually as the loading amount is increased from 4 to 6 $\text{mg}/\mu\text{L}$, but as the loading is increased to 8 $\text{mg}/\mu\text{L}$, the current response decreases. This indicates that the formation of a large number of molecules over the electrode surface causes the GCE to reach its saturation point at 8 $\text{mg}/\mu\text{L}$, and the passivation effect and coating thickness have an impact on this outcome. Thus, a perfect concentration of 6 $\text{mg}/\mu\text{L}$ was determined and is used in further studies.

3.7.3. Effect of Various pH

At various electrolyte pH ranges (basic, neutral, and acidic), the modified surface of the electrode significantly affects the oxidation current potential. Because $\text{CePO}_4/f\text{-CNF}$

has active functional groups on its surface, the pH of the solution had adverse effects on the material's surface. Figure 5C,D shows the CV graphs of $\text{CePO}_4@f\text{-CNF}/\text{GCE}$ with 100 μM of HXA at a scan rate of 50 mV/s under pH values ranging from pH 3–11 in 0.1 M PB solution. The slight rise in oxidation peak current values between pH 3 to 7 and the gradual reduction from pH 7–11 is attributed to the preference for the movement of protons in electrolyte functional groups. In acidic conditions, a relatively small oxidation peak current demonstrates that the large amounts of protons within the suspension restrict the movement of electrons, which results in better conductivity. This suggests that HXA is pH-dependable in electrochemical sensors and that electrochemical analysis is optimal at pH 7. Since this sensor device's electrode operation has improved at neutral pH, it is optimal for evaluation in real samples. According to the previously reported work, a plausible mechanism for the electrooxidation of HXA was proposed. Here, the HXA reaction would seem to be a $-2\text{H}^+ + 2\text{e}^-$ oxidation of HXA to 6,8-dioxypurine at the N7 = C8 double bond [31], as shown in Figure S4.

3.7.4. Different Concentrations of HXA and Scan Rates

In the CV approach, the performance of the $\text{CePO}_4@f\text{-CNF}/\text{GCE}$ -modified electrode at various HXA concentrations was measured. The CV characteristics at a scan rate of 50 mV/s are shown in Figure 5E, ranging from 25 to 125 μM of HXA in 0.1 M of PB aqueous solution. When increasing the HXA concentration, there was also a gradual and linearly increase in the oxidation peak current, which established the increased conductivity of ions of the modified GCE as revealed by the raised level of HXA. The prepared nanocomposite achieves a suitable electrolyte for rapid electron transfer, which encourages the electrochemical reaction and improves the peak current. Furthermore, the rise in the peak current demonstrates the $\text{CePO}_4@f\text{-CNF}/\text{GCE}$ antifouling properties. Additionally, the linear correlation between the concentration of the solution and the irreversible redox peak current response is shown in Figure 5E (inset picture), with obtained regression equations of $I_{\text{pa}} = 0.0673x + 1.7568$ and R^2 values of 0.9962 (oxidation). The CV curves for HXA detected by $\text{CePO}_4@f\text{-CNF}/\text{GCE}$ consist of a single oxidation peak, as shown in Figure 5F, suggesting that HXA exhibits an irreversible oxidation reaction. Furthermore, the peak current of the CV curve progressively rises while the scan rate increases from 0.02 to 0.2 V/s. Additionally, the irreversible redox peak current response and the scan rate are displayed to be linearly correlated in Figure 5F (inset graph), with the R^2 values of 0.9924 and the derived regression equations of $I_{\text{pa}} = 16.997x + 2.2613$. Thus, the $\text{CePO}_4@f\text{-CNF}/\text{GCE}$ -modified electrode predicted that scan rates would show an absorption-controlled process.

3.8. Determination of Calibration Plot and Limit of Detection

The analytical amount for $\text{CePO}_4@f\text{-CNF}/\text{GCE}$ -modified GCE was obtained via differential pulse voltammetry (DPV) to detect HXA using electrochemical measurements. Figure 6A displays the DPV of anodic peak currents that cause the oxidation of HXA at potential 1.02 V. As the concentration increases from 0.1 to 629 μM , the anodic current also increases uniformly. Increasing the low to high concentration of HXA results in a strong peak current response, which indicates the better conductivity of both CePO_4 and $f\text{-CNF}$. Figure 6B shows a linear calibration line for the DPV current and concentration. The regression equation estimated is given as $I_{\text{pa}} = -0.0579x + 6.7055$ with a regression coefficient of $R^2 = 0.9919$. The prepared device's diagnostic properties were analyzed through a limit of detection (LOD) of 0.23 μM , and it was calculated by using $\text{LOD} = 3 \times (\text{standard deviation of low concentration}) / (\text{slope of the calibration plot})$ [32–34] in the wide linear ranges of 2.05–629 μM , shown in Table S3. The results from this study demonstrate that the synthesized $\text{CePO}_4@f\text{-CNF}$ does not simply have a smaller detection limit, but also has a larger linear range for HXA sensing.

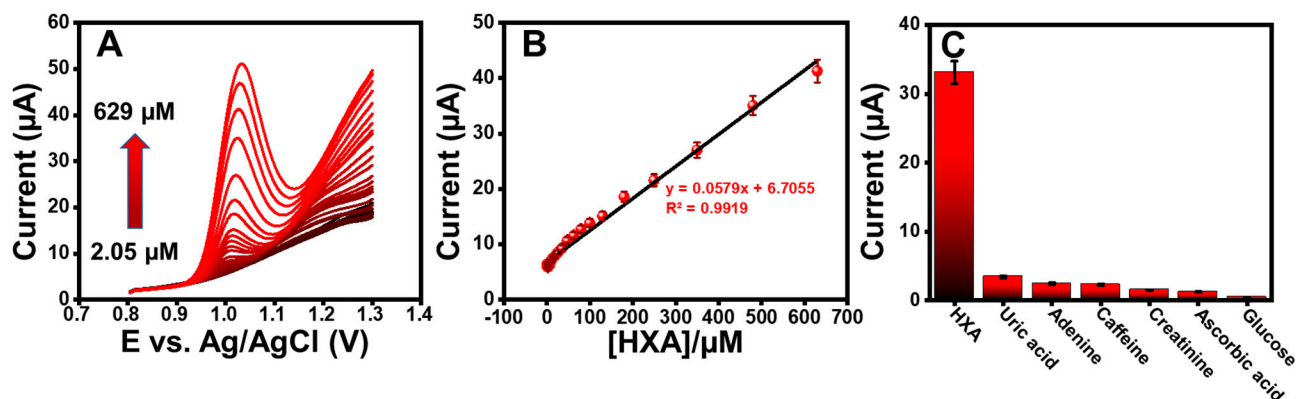


Figure 6. (A) DPV measurements for accelerating the deposition of HXA into the CePO₄@f-CNF/GCE. (B) Calibration plot for the current acquired with the increment of HXA. (C) Interference study of various analytes over HXA.

3.9. Selectivity Studies

The sensor system has to determine hypoxanthine in the presence of other analytes. To test the selectivity of the CePO₄@f-CNF/GCE-modified electrode, extra quantities of interference chemical compounds like Uric acid, Adenine, Caffeine, Creatinine, Ascorbic acid, and Glucose were added toward the electrolyte solution along with HXA. Figure 6C shows the negligible effect of interfering substances, suggesting that HXA has overcome the overlapping effect of other compounds. As a result, the suggested sensor has an appropriate amount of selectivity for HXA detection. CV analysis of the CePO₄@f-CNF/GCE examined the repeatability, displayed in Figure S2A,B., indicating excellent repeatability of the synthesized nanocomposite as determined by the results, which reveals a significant similarity between the peak current and relative standard deviation of all four electrodes. These outcomes demonstrate that there was no impact on the peak current of the CePO₄@f-CNF-modified GCE, including the 100 μM/mg HXA analyte. Furthermore, the stability studies of the CePO₄@f-CNF/GCE on HXA were carried out by calculating the peak current approximately similar between 30 cycles with a bar diagram displayed in Figure S3A,B. This bar diagram confirmed the current decreased by below 10% from the first cycle to the 30th cycle. Based on the results, we confirmed that CePO₄@f-CNF shows better stability towards the detection of HXA.

3.10. Practical Applicability

Additionally, we analyzed real samples to confirm the modified electrode's reliability. When the obtained samples were analyzed using the DPV method to get an un-spiked HXA pick, no current response was displayed (Figure 7A,B). After mixing an HXA concentration (5, 10, 15, and 20 μM of 0.01 μM/mg solution of the analyte), a response was found concerning the expected current, and also the observed LOD values of chicken and fish samples were 0.8 and 0.6 μM in real sample analysis. The newly developed electrode exhibited better recovery ranges, demonstrating that it is a suitable as well as beneficial platform for measuring HXA in fish and chicken samples. The prepared sensor shows that the expectational recovery and intense practicality are demonstrated using the detection of HXA in the real sample.

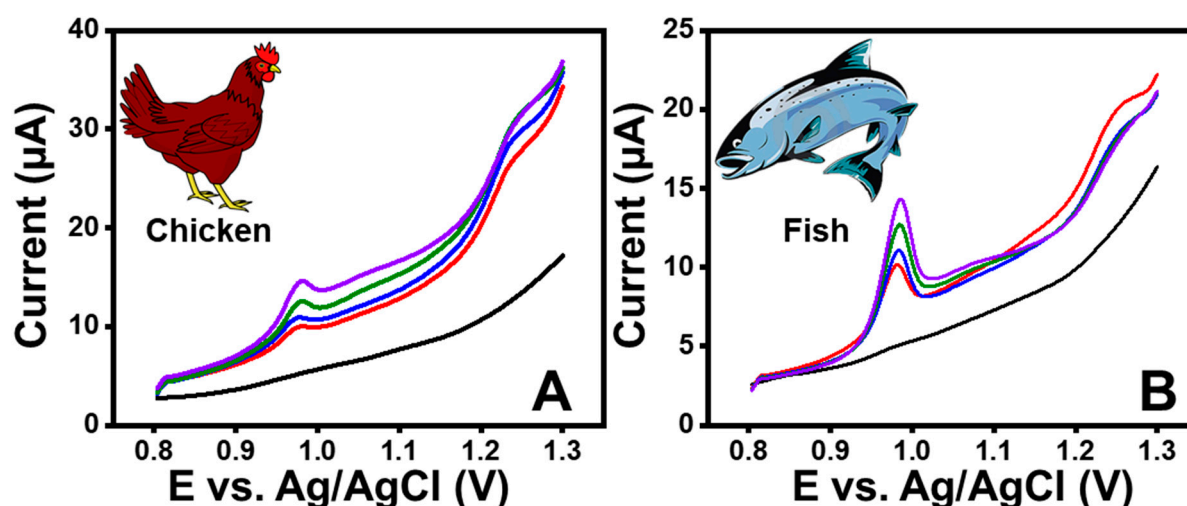


Figure 7. DPV reading of $\text{CePO}_4@f\text{-CNF}/\text{GCE}$ in the presence of HXA: (A) chicken, (B) fish sample.

4. Conclusions

In summary, we synthesized a $\text{CePO}_4@f\text{-CNF}$ nanocomposite using a facile hydrothermal and sonication approach and used it for efficient electrochemical HXA detection. The successful formation of a $\text{CePO}_4@f\text{-CNF}$ nanocomposite was confirmed through morphological and spectroscopic analysis. The synergism between CePO_4 and $f\text{-CNF}$ shows high electron transfer efficiency and a large specific surface area, which gives wide linear ranges, lower electrode/electrolyte resistance, low limits of detection, and good electrochemical stability, which are necessary for electrochemical sensors. Furthermore, using CV and DPV techniques, the electrochemical activity of $\text{CePO}_4@f\text{-CNF}$ for the detection of HXA was determined, exhibiting the nanocomposite material's enhanced catalytic behavior. In addition, the proposed sensor gives significant stability (30 cycles), good LOD at $0.23 \mu\text{M}$, repeatability with four repeated measurements, and selectivity with seven interfering substances. Hence, the $\text{CePO}_4@f\text{-CNF}$ nanocomposite depicts superior electrochemical performance towards HXA determination. A good HXA-spiked response was observed by using $\text{CePO}_4@f\text{-CNF}$ -modified electrodes in real-life samples with fish and chicken.

Supplementary Materials: The following Supporting Information can be downloaded at <https://www.mdpi.com/article/10.3390/chemosensors12050084/s1>, Figure S1: (A) CV curves for various loading amounts of $\text{CePO}_4@f\text{-CNF}$ towards the detection of hypoxanthine in 0.1 M PB (pH-7.0). (B) Respective bar diagram for various loading amounts; Figure S2: (A) and (B) CV curves for a repeatability study towards HXA in electrolyte PB (pH-7.0) and respective bar diagram; Figure S3: (A and B). Cycle stability of $\text{CePO}_4@f\text{-CNF}$ with the presence of hypoxanthine, with a bar diagram; Figure S4: Possible electro-oxidation mechanism of hypoxanthine; Table S1: Crystallographic analysis of CePO_4 peak position ($2\theta^\circ$) and lattice planes (hkl) value; Table S2: Summarized R_{ct} values obtained from different modified electrodes; Table S3: Comparison of the proposed method with other electrochemical methods for the determination of HX. References [35–42] are cited in the supplementary materials.

Author Contributions: S.-F.W.: Validation, Conceptualization, Resources, Data Curation, Supervision, Funding acquisition, Writing—Review and Editing. P.K.K.: Writing—Original Draft, Methodology, Investigation, Formal Analysis, Visualization, Data Curation. All authors have read and agreed to the published version of the manuscript.

Funding: This research was funded by National Taipei University of Technology (NTUT).

Institutional Review Board Statement: Not applicable.

Informed Consent Statement: Not applicable.

Data Availability Statement: Data is contained within the article and the Supplementary Materials.

Acknowledgments: This work was financially supported by the National Taipei University of Technology (NTUT).

Conflicts of Interest: The authors declare no competing financial interest.

References

1. Garg, D.; Singh, M.; Monika, N.V. Review on recent advances in fabrication of enzymatic and chemical sensors for hypoxanthine. *Food Chem.* **2022**, *375*, 131839. [[CrossRef](#)]
2. King, M.E.; Honeysett, J.M.; Howell, S.B. Regulation of de novo purine synthesis in human bone marrow mononuclear cells by hypoxanthine. *J. Clin. Investig.* **1983**, *72*, 965–970. [[CrossRef](#)] [[PubMed](#)]
3. Dey, B.; Ahmad, W.; Sarkhel, G.; Lee, G.H.; Choudhury, A. Fabrication of niobium metal organic frameworks anchored carbon nanofiber hybrid film for simultaneous detection of xanthine, hypoxanthine and uric acid. *Microchem. J.* **2023**, *186*. [[CrossRef](#)]
4. Nakatani, H.S.; Santos, L.V.D.; Pelegrine, C.P.; Gomes, S.T.M.; Matsushita, M.; de Souza, N.E.; Visentainer, J.V. Biosensor Based on Xanthine Oxidase for Monitoring Hypoxanthine in Fish Meat. *Am. J. Biochem. Biotechnol.* **2005**, *1*, 85–89. [[CrossRef](#)]
5. Torres, R.J.; Prior, C.; Garcia, M.G.; Puig, J.G. A review of the implication of hypoxanthine excess in the physiopathology of Lesch–Nyhan disease. *Nucleosides Nucleotides Nucleic Acids* **2016**, *35*, 507–516. [[CrossRef](#)] [[PubMed](#)]
6. Jiang, Z.; Dong, H.; Zhou, Y.; Chen, Y.; Hao, W.; Zhang, Z.; Hao, Y.; Liu, L.; Wang, X.; Xu, M. Simultaneous and Ratiometric Electrochemical Determination of Uric Acid and Hypoxanthine Based on In Situ Carbonized Polydopamine Graphene Paper. *ACS Appl. Nano Mater.* **2023**, *6*, 9268–9275. [[CrossRef](#)]
7. Peter, J.N.; Ulse, N.P.; Ole, T.; Num, R.; Eph, S.T.; Oyasjet, A.; Oi, A.D. Changes in Oxypurine Concentrations in Vitreous Humor of Pigs during Hypoxemia and Post-Mortem. *Pediatr. Res.* **1990**, *28*, 482–484.
8. Cao, Y.; Song, Y.; Wei, T.; Feng, T.; Li, M.; Xue, C.; Xu, J. MnO₂ in-situ coated upconversion nanosystem for turn-on fluorescence detection of hypoxanthine in aquatic products. *Food Chem.* **2024**, *431*, 137131. [[CrossRef](#)]
9. Mustafa, F.; Andreescu, S. Paper-Based Enzyme Biosensor for One-Step Detection of Hypoxanthine in Fresh and Degraded Fish. *ACS Sens.* **2020**, *5*, 4092–4100. [[CrossRef](#)]
10. Pu-Werman, G.J.; Shaikh, B.; Hallmark, M.R.; Sawyer, C.G.; Hixson, C.V.; Perini, F. Simultaneous Analysis of Substrates, Products, and Inhibitors of Xanthine Oxidase by High-Pressure Liquid Chromatography and Gas Chromatography. *Anal. Biochem.* **1979**, *98*, 18–26.
11. Khandagale, D.D.; Wang, S.F. Fabrication of tin sulfide@functionalized carbon nanofiber composites for the electrochemical detection of the oxidative stress biomarker trolox. *New J. Chem.* **2023**, *47*, 14933–14942. [[CrossRef](#)]
12. Xia, Y.; Calahoo, C.; Rodrigues, B.P.; Griebenow, K.; Graewe, L.; Wondraczek, L. Structure and properties of cerium phosphate and silicophosphate glasses. *J. Am. Ceram. Soc.* **2023**, *106*, 2808–2819. [[CrossRef](#)]
13. Feng, N.; Liu, Y.; Dai, X.; Wang, Y.; Guo, Q.; Li, Q. Advanced applications of cerium oxide based nanozymes in cancer. *RSC Adv.* **2022**, *12*, 1486–1493. [[CrossRef](#)] [[PubMed](#)]
14. Altass, H.M.; Khder, A.S.; Ahmed, S.A.; Morad, M.; Alsabei, A.A.; Jassas, R.S.; Althagafy, K.; Ahmed, A.I.; Salama, R.S. Highly efficient, recyclable cerium-phosphate solid acid catalysts for the synthesis of tetrahydrocarbazole derivatives by Borsche–Drechsel cyclization. *React. Kinet. Mech. Catal.* **2021**, *134*, 143–161. [[CrossRef](#)]
15. Kushwaha, A.; Singh, G.; Sharma, M. Designing of cerium phosphate nanorods decorated reduced graphene oxide nanostructures as modified electrode: An effective mode of dopamine sensing. *Microchem. J.* **2021**, *166*, 106224. [[CrossRef](#)]
16. Kim, S.; Choi, M.; Park, J. Cerium-Doped Oxide-Based Materials for Energy and Environmental Applications. *Crystals* **2023**, *13*, 1631. [[CrossRef](#)]
17. Yoon, J.H.; Jinsoo, B.; Cho, I.; Vinodh, R.; Pollet, B.G.; Babu, R.S.; Kim, H.J.; Kim, S. Novel Supercapacitor Electrode Derived from One Dimensional Cerium Hydrogen Phosphate (1D-Ce(HPO₄)₂·xH₂O). *Molecules* **2022**, *27*, 7691. [[CrossRef](#)] [[PubMed](#)]
18. Varun, D.N.; Manjunatha, J.G.; Hareesha, N.; Sandeep, S.; Mallu, P.; Karthik, C.S.; Prinitih, N.S.; Sreeharsha, N.; Asdaq, S.M.B. Simple and sensitive electrochemical analysis of riboflavin at functionalized carbon nanofiber modified carbon nanotube sensor. *Monatshefte Für Chem.–Chem. Mon.* **2021**, *152*, 1183–1191. [[CrossRef](#)]
19. Marenco, A.J.; Pillai, R.G.; Harris, K.D.; Chan, N.W.; Jemere, A.B. Electrochemical Determination of Fentanyl Using Carbon Nanofiber-Modified Electrodes. *ACS Omega* **2024**, *9*, 17592–17601. [[CrossRef](#)]
20. Bharathi, P.; Wang, S.F. Strontium phosphate/functionalized carbon nanofiber composite: A promising electrode material for amperometric detection of flufenamic acid. *Process Saf. Environ. Prot.* **2023**, *178*, 642–651. [[CrossRef](#)]
21. Periyasamy, S.; Lee, C.H.; Fu, C.C.; Liu, S.H.; Juang, R.S. Ultrasound-assisted synthesis of barium tungstate encapsulated carbon nanofiber composite for real-time sensing of p-cresol in human urine samples. *Microchem. J.* **2021**, *166*, 106239.
22. Cui, L.; Yang, Y.; Jiang, S.; Cao, X.; Chu, W.; Chen, J.; Sun, B.; Ren, K.; Zhang, C.Y. Exogenous Co-Reactant-Free Electrochemiluminescent Biosensor for Ratiometric Measurement of α -Glucosidase Based on a ZIF-67-Regulated Hydrogen-Bonded Organic Framework. *ACS Sens.* **2024**, *9*, 1023–1030. [[CrossRef](#)]
23. Dalapati, R.; Biswas, S. A pyrene-functionalized metal–organic framework for nonenzymatic and ratiometric detection of uric acid in biological fluid via conformational change. *Inorg. Chem.* **2019**, *58*, 5654–5663. [[CrossRef](#)] [[PubMed](#)]
24. Rajesh, K.; Mukundan, P.; Pillai, P.K.; Nair, V.R.; Warriar, K.G.K. High-surface-area nanocrystalline cerium phosphate through aqueous sol-gel route. *Chem. Mater.* **2004**, *16*, 2700–2705. [[CrossRef](#)]

25. Zhu, K.; Chao, X.F.; Liu, Y.; Luo, Y.H.; Zhang, Q.Y.; Zhao, Z.A.; Zhu, Q.; Chen, F.Y.; Zhang, D.E. Facial Construction of CePO₄-Reduced Graphene Oxide Composite for Enhanced Electrochemical Detection of Dopamine and Acetaminophen. *J. Electrochem. Soc.* **2022**, *169*, 067505. [[CrossRef](#)]
26. Navarro-Jaén, S.; Romero-Sarria, F.; Centeno, M.A.; Laguna, O.H.; Odriozola, J.A. Phosphate-type supports for the design of WGS catalysts. *Appl. Catal. B* **2019**, *244*, 853–862. [[CrossRef](#)]
27. Kirubanithy, M.; Irudayaraj, A.A.; Raj, A.D.; Manikandan, S. Synthesis, characterization and photoluminescence behaviours of CePO₄ and Tb-doped CePO₄ nanostructures. *Mater. Today Proc.* **2015**, *2*, 4344–4347. [[CrossRef](#)]
28. Asuvathraman, R.; Gnanasekar, K.I.; Clinsha, P.C.; Ravindran, T.R.; Kutty, K.G. Investigations on the charge compensation on Ca and U substitution in CePO₄ by using XPS, XRD and Raman spectroscopy. *Ceram. Int.* **2015**, *41*, 3731–3739. [[CrossRef](#)]
29. Sriram, B.; Govindasamy, M.; Wang, S.F.; Joseph, X.B. A ternary nanocomposite based on nickel (iii) oxide@ f-CNF/rGO for efficient electrochemical detection of an antipsychotic drug (*Klonopin*) in biological samples. *New J. Chem.* **2020**, *44*, 10250–10257. [[CrossRef](#)]
30. Subbiah, K.D.; Nesakumar, N.; Kulandaisamy, A.J.; Rayappan, J.B. Ferricyanide/reduced graphene oxide as electron mediator for the electrochemical detection of methanol in canned citrus sinensis and citrus limetta. *Sens. Actuators B Chem.* **2017**, *248*, 708–717. [[CrossRef](#)]
31. Wei, M.J.; Lu, X.Y.; Li, J.; Kong, F.Y.; Zhou, J.; Wang, Z.X.; Wang, W. Coupling highly conductive covalent organic framework with nitrogen doped carbon nanotubes enables simultaneous and sensitive quantification of xanthine and hypoxanthine. *Microchem. J.* **2023**, *194*, 109205. [[CrossRef](#)]
32. Ramanathan, S.; Elanthamilan, E.; Obadiah, A.; Durairaj, A.; Santhoshkumar, P.; Merlin, J.P.; Ramasundaram, S.; Vasanthkumar, S. Electrochemical Detection of Trace Amounts of Arsenic (III) in Poultry Using a Graphene Oxide-Bis(2-(4,5-diphenyl-1H-imidazol-2-yl)phenoxy)Cobalt Composite Modified Electrode. *J. Electron. Mater.* **2019**, *48*, 4498–4506. [[CrossRef](#)]
33. Cecilia, C.; Palchetti, I.; Mascini, M.; Parenti, A. Electrochemical sensor and biosensor for polyphenols detection in olive oils. *Food Chem.* **2000**, *71*, 553–562.
34. Zhao, C.; Chen, M.; Liu, X.; Yuan, W.; Li, K.; Wang, Y.; Chen, C.; Zhang, M.; Dong, Y.; Xiao, Y.; et al. Direct single-molecule detection of CoA-SH and ATP by the membrane proteins TMEM120A and TMEM120B. *Nanoscale* **2024**, *16*, 6087–6094. [[CrossRef](#)] [[PubMed](#)]
35. Vishnu, N.; Gandhi, M.; Rajagopal, D.; Kumar, A.S. Pencil graphite as an elegant electrochemical sensor for separation-free and simultaneous sensing of hypoxanthine, xanthine and uric acid in fish samples. *Anal. Methods* **2017**, *9*, 2265–2274. [[CrossRef](#)]
36. Lavanya, N.; Sekar, C.; Murugan, R.; Ravi, G. An ultrasensitive electrochemical sensor for simultaneous determination of xanthine, hypoxanthine and uric acid based on Co doped CeO₂ nanoparticles. *Mater. Sci. Eng. C* **2016**, *65*, 278–286. [[CrossRef](#)] [[PubMed](#)]
37. Kumar, A.S.; Swetha, P. Ru(DMSO)₄Cl₂ nano-aggregated Nafion membrane modified electrode for simultaneous electrochemical detection of hypoxanthine, xanthine and uric acid. *J. Electroanal. Chem.* **2010**, *642*, 135–142. [[CrossRef](#)]
38. Kumar, S.A.; Shanmugam, R. Simple method for simultaneous detection of uric acid, xanthine and hypoxanthine in fish samples using a glassy carbon electrode modified with as commercially received multiwalled carbon nanotubes. *Anal. Methods* **2011**, *3*, 2088–2094. [[CrossRef](#)]
39. Thangaraj, R.; Kumar, A.S. Graphitized mesoporous carbon modified glassy carbon electrode for selective sensing of xanthine, hypoxanthine and uric acid. *Anal. Methods* **2012**, *4*, 2162–2171. [[CrossRef](#)]
40. Dou, Z.Y.; Cui, L.L.; He, X.Q. Electrochemical determination of uric acid, xanthine and hypoxanthine by poly(xylitol) modified glassy carbon electrode. *J. Cent. South Univ.* **2014**, *21*, 870–876. [[CrossRef](#)]
41. Zen, M.; Lai, Y.; Yang, H.; Kumar, A.S. Multianalyte sensor for the simultaneous determination of hypoxanthine, xanthine and uric acid based on a preanodized nontronite-coated screen-printed electrode. *Sens. Actuators B Chem.* **2002**, *84*, 237–244. [[CrossRef](#)]
42. Raj, M.A.; John, S.A. Simultaneous determination of uric acid, xanthine, hypoxanthine and caffeine in human blood serum and urine samples using electrochemically reduced graphene oxide modified electrode. *Anal. Chim. Acta* **2013**, *771*, 14–20. [[CrossRef](#)] [[PubMed](#)]

Disclaimer/Publisher’s Note: The statements, opinions and data contained in all publications are solely those of the individual author(s) and contributor(s) and not of MDPI and/or the editor(s). MDPI and/or the editor(s) disclaim responsibility for any injury to people or property resulting from any ideas, methods, instructions or products referred to in the content.